The influence of temperature on the deformation behavior, strength and fracture mechanism of the heat-resistant Nickel-based alloy EI698-VD

Aleksandr Sulamanidze
Institute of Power Engineering and Advanced Technologies, FRC Kazan Scientific Center, Russian Academy of Sciences, Russia
AGSulamanidze@gmail.com, http://orcid.org/0000-0002-8420-0354

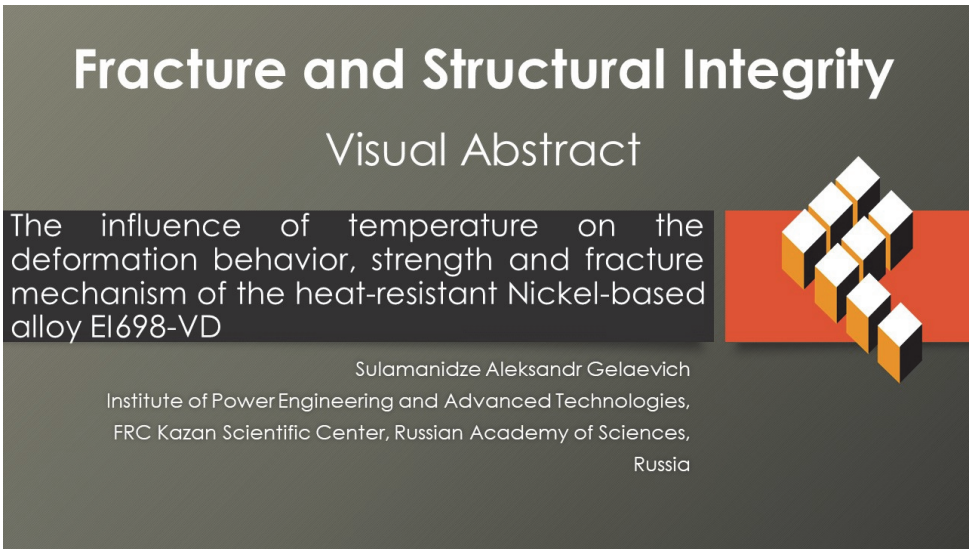

Citation: Sulamanidze, The influence of temperature on the deformation behavior, strength and fracture mechanism of the heat-resistant Nickel-based alloy EI698-VD, Fracture and Structural Integrity, 76 (2026) 154-168.

Received: 05.12.2025
Accepted: 04.02.2026
Published: 05.02.2026
Issue: 04.2026

KEYWORDS. Nickel-based alloy XH73MBTU-VD (EI698-VD), Plasticity, Strength, Crack, Dislocation slip bands, Fracture analysis.

INTRODUCTION

Components produced from heat-resistant nickel alloys are exposed to monotonic or cyclic loading. Concurrently, the material is subjected to damaging external factors, including elevated and cyclically changing temperatures. The behaviour of materials under these conditions is subject to variation, with the potential to significantly impact performance and service life. In order to design components and structures correctly, and to determine stress-strain states and predict durability, it is necessary to obtain complete and accurate data on the behaviour of the material under the relevant operating conditions.

The nickel-based polycrystalline alloy XH73MBTU-VD (EI698-VD) is used in the power industry and aviation at temperatures of up to 750°C. GTE turbine discs are made from the EI698-VD alloy. There have been documented cases of surface cracks and failure in service of GTE turbine components made from the EI698-VD alloy [1]. Furthermore, it was observed that when the EI698-VD alloy was maintained at elevated temperatures (in excess of 400 °C) for extended

periods without the action of an external load, inelastic shrinkage and swelling strain occurred [2]. These phenomena were accompanied by strain oscillations.

In [3], an overview of the characteristics of the EI698-VD alloy structure and the features of its behaviour in operation was previously presented. In this section, the primary characteristics of the alloy under consideration are outlined. The heat-resistant nickel-based alloy EI698-VD is dispersion-strengthened. During the process of cooling, a strengthening γ'-phase is released from the nickel-based γ matrix with a BCC lattice [4, 5]. According to [6], the grain size is approximately 30-60 μm. Large MC carbides are embedded inside the grain, and small $M_{23}C_6$ carbides are located at the grain boundaries [7]. The γ'-phase particles are spherical in shape, with a large particle size of 0.2–0.6 μm [6,7,8]. The mass fraction of the γ'-phase in the alloy is 20.5% [9]. According to the measurements reported in [10], the primary spherical γ' particles have a size of approximately 0.06 μm, and their volume fraction was estimated to be around 35%.

In the preceding studies on fatigue crack growth rate in the temperature range of 25–650°C and under thermomechanical conditions, a change in the fracture mechanism was observed from transgranular to intergranular at temperatures above 400°C [11]. An attempt to numerically reproduce this process within the frame of the finite element method was made in [12]. Furthermore, when this temperature threshold was exceeded, the fatigue crack growth rate increased significantly [3]. It is important to note that the model based on the energy fracture resistance parameter, the damage impact parameter A introduced by Sulamanidze [3], demonstrated the capacity to predict fatigue crack growth, taking into account the rapid degradation of properties as the temperature rises, as well as under thermomechanical conditions of cyclic loading. The input data for numerical finite element analysis [13, 14], on the basis of which the values of the damage impact parameter A were determined, were the results of tests on uniaxial monotonic tension in the temperature range of fatigue crack growth. Consequently, it can be assumed that the mechanisms controlling the degradation of fatigue crack growth characteristics with increasing temperature are related to the mechanisms controlling the decrease in strength and plasticity characteristics under uniaxial monotonic loading. The present study aims to analyse the deformation behaviour and microstructure of specimens made of the nickel-based alloy EI698-VD, with a view to proposing possible causes for the rapid decrease in characteristics and the change in the fracture mechanism with increasing temperature.

MATERIALS AND METHODS

The behaviour of the EI698-VD alloy was studied under elevated temperatures in the range of 25–700°C. Cylindrical specimens (Fig. 1) were cut from hot-rolled bar. The nominal composition of the EI698-VD alloy is given in Tab. 1. The specimens were tested using the UTS111 testing setup (Fig. 1), which is equipped with an Epsilon high-temperature extensometer and a high-temperature furnace.

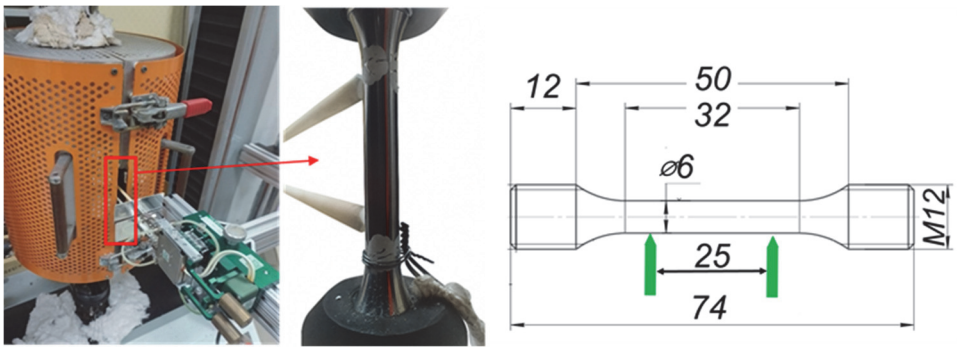

Figure 1: UTS111 test setup and specimen sketch. A smooth cylindrical specimen with a diameter of 6 mm is placed in a three-zone furnace. A K-type thermocouple is attached to the specimen. High-temperature extensometer blades with a gauge length of 25 mm are attached to the specimen.

	C	Cr	Ti	Al	Mo	Fe	Ni	B
wt.%	0.03…0.07	13…16	2.37…2.75	1.45…1.8	2.8…3.2	<2	Bal.	≤0.005
	Si	Mn	S	P	Ce	Pb	Nb	
wt.%	≤0.5	≤0.4	≤0.007	≤0.015	≤0.005	≤0.001	1.9…2.2	

Table 1: Nominal chemical composition of alloy EI698-VD.

The objective of this study is to conduct a series of short-term tests at temperatures ranging from 25 to 700 °C. In monotonic tensile tests until fracture, the specimen was fixed in the upper and lower rods of the UTS111 test frame. The specimen was heated to a temperature T and maintained for 1.5 h at a load of 200 N before the main load was applied. The load was applied in a displacement control mode with a constant displacement rate of 1 mm/min (Fig. 2).

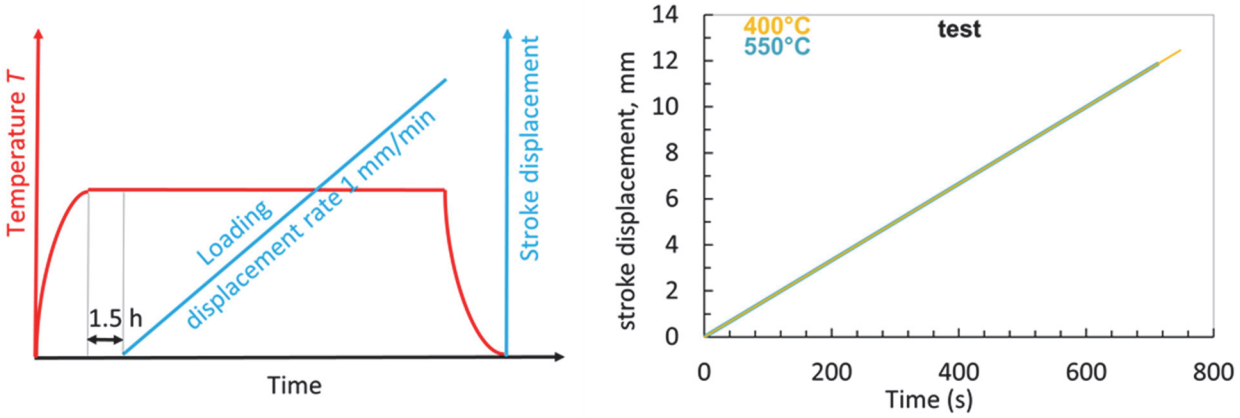

Figure 2: Testing procedure for monotonic tensile at elevated temperatures. The specimen was heated in a furnace to a target temperature T. After holding at temperature T for 1.5 h, loading was initiated at a displacement rate of 1 mm/min.

The UTS111 test setup is equipped with a three-zone high-temperature furnace that can maintain a constant temperature of up to 1200°C. The air temperature was measured by three N-type thermocouples positioned within the specimen area. The surface temperature of the specimen in the furnace was measured with a K-type thermocouple (Fig. 1). The axial ε_Y strains were measured using a high-temperature Epsilon extensometer with a 25 mm gauge length (Fig. 1). The experimental data, which included strain, force, traverse displacement, and T, were recorded from the beginning of the test until fracture. The fractured specimen images were analysed in CAE applications to measure the slip plane angle. In the CAE application, the specimen axis was defined as the midline between the cylindrical surface contours. The mean-square deviation is calculated based on measurements of the slope angles of five slip planes.
The microstructure of the alloy was characterised using a Zeiss Merlin scanning electron microscope (SEM), which was equipped with an Oxford X-max 80 energy-dispersive X-ray (EDX) detector for elemental analysis. Discs with a thickness of 3 mm and a diameter of 11 mm were cut from the specimens, as was previously described in [15]. For the SEM, the cut discs were polished to 0.1 μm.

RESULTS AND DISCUSSION

The properties of alloy EI698-VD are outlined in Tab. 2 [13, 14]. In this table, E is the Young's modulus, σ_y is the yield stress, σ_u is the ultimate tensile strength, σ_f is the true rupture strength (see Eqn. 1), ε_f (see Eqn. 2) and ε_{fe} are true and engineering rupture strains, and ψ_{en} (see Eqn. 3) is relative reduction. ω_f and ω_{fe} are the critical strain energy density, which are obtained as the area under the true and engineering stress-strain curve [3].

$$\sigma_f = (P_f / F_0) / (1 - \psi_{en}) \quad (1)$$

$$\varepsilon_f = (\ln / (1 - \psi_{en})) \cdot 100\% \quad (2)$$

$$\psi_{en} = (F_0 - F_f) / F_0 \quad (3)$$

where F_0, F_f are the cross-sectional areas of the specimen before and after the test, and P_f is the force at the moment of rupture [16].
The data presented in Fig. 3 [13] and Tab. 2 demonstrate that an increase in temperature results in a decrease in the strength and plasticity of the alloy, specifically the critical strain energy density, ultimate tensile strength, and rupture strain. When

the temperature exceeds 550 °C, the values of rupture strain decrease sharply. However, for the nominal characteristics of alloy EI698-VD [17], the rupture strain for temperatures of 20, 500, 600, 650, and 700 °C is 31, 31, 28, 28, and 24 %, respectively.

T, °C	E, MPa	σ_y, MPa	σ_u, MPa	σ_f, MPa	ε_f, %	ε_{fe}, %	ψ_{en}, %	ω_{fe}, MJ·m^{-3}	ω_f, MJ·m^{-3}
25	214480	909.57	1306.11	2530.65	77.04	35	54	415.63	1563.61
400	203780	829.95	1229.52	2036.73	71.09	32.3	50.8	351.91	1240.40
550	206180	836.42	1205.93	1944.55	69.91	27.7	50.3	290.04	1189.92
650	189236	868.09	1078.97	1249.33	18.40	11.1	16.8	101.24	224.76
700	174000	897.62	1035.35	1074.78	12.02	6.14	11	55.49	126.26

Table 2: Characteristics of alloy EI698-VD in the temperature range 25-700 °C obtained in tests.

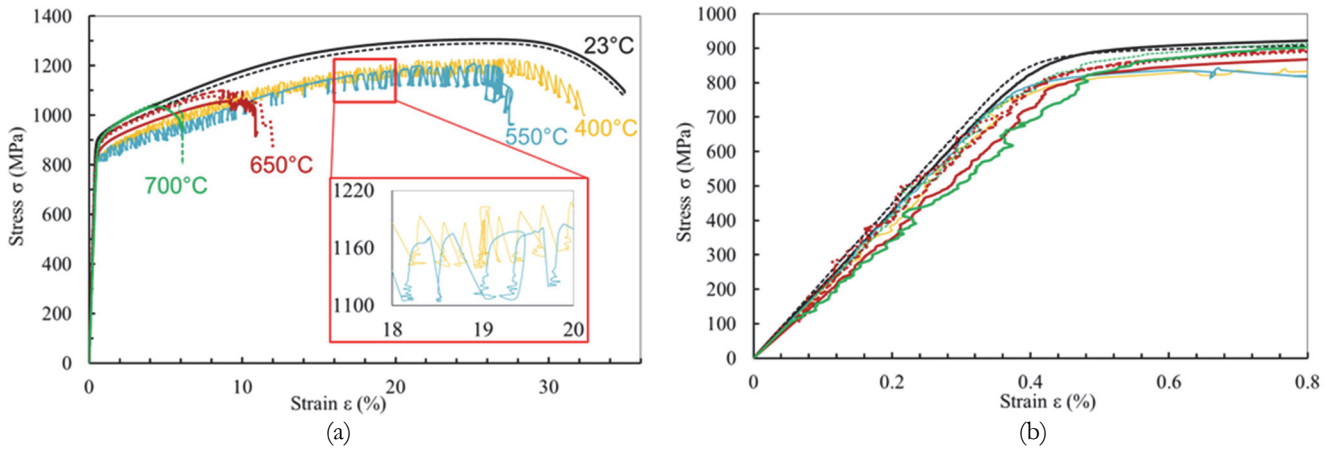

Figure 3: (a); engineering stress-strain curves for alloy EI698-VD in the temperature range 25–700°C and (b); range of elastic strain. At temperatures of up to 550°C, the tested alloy demonstrates a high level of plasticity. A subsequent increase in temperature, ranging from 650 to 700°C, has been observed to result in a significant decrease in rupture strain. The PLC effect was observed at temperatures ranging from 400 to 700°C.

Serrated flow effect

As demonstrated in Fig. 3a, the "serrated flow" effect, also referred to as the Savatry-Masson or Porteven-Le Chatelier (PLC) effect, occurred at a temperature of 400 °C. The serrated flow effect has been observed to be associated with negative strain-rate sensitivity and the interaction of dislocations with impurity atoms [18,19,20]. Impurity atoms are fixed on dislocations, thereby limiting their movement due to the slower diffusion mechanism of atom movement. The increase in yield stress that was observed with rising temperature (400-700°C, see Tab. 2) had previously been attributed by the authors [21] to the PLC effect. The behavior of the material at temperatures of 650 and 700 °C corresponds to serrated flow type C [22,23], since stress drops do not appear at the initial stage of the elastic-plastic section of the tensile curve. Type C is also often observed at higher temperatures. In this case, localized strain bands originate with high stress drop values. At a temperature of 400 °C, serrated flow occurs throughout the entire elastic-plastic deformation, which corresponds to type B.

It can be seen that during serrated flow, in sections where the load increases between stress drops, the strain rate rapidly increases (Fig. 4). The strain rate for 400 and 550 °C at the moment of stress drops is approximately constant throughout the entire tensile curve and is equal to about (5…9)·10^{-4} sec^{-1} (Fig. 4). For 23, 650, and 700 °C, the strain rate was about (4...5)·10^{-4} sec^{-1} (Fig. 5) without serrated flow. As is known, the diffusion rate of atoms increases with temperature. It can be seen that for 650 and 700 °C, serrated flow appears under conditions of increased strain rate values. At a temperature of 650 °C, the strain rate at the onset of serrated flow was 6·10^{-4} sec^{-1} (ε = 8.5 %), and at a temperature of 700 °C, it was 7·10^{-4} sec^{-1} (ε = 6 %). Therefore, based on the concept of the PLC effect mechanism, it can be assumed that strain at a strain rate of (4...5)·10^{-4} sec^{-1} for temperatures of 650 and 700 °C enabled impurity atoms to move together with dislocations until the strain rate increased further. It can then be supposed that at 400 and 550 °C, the strain rate at which the stress drop occurred (5…9)·10^{-4} sec^{-1} is the upper limit for the movement of impurity atoms fixed on dislocations.

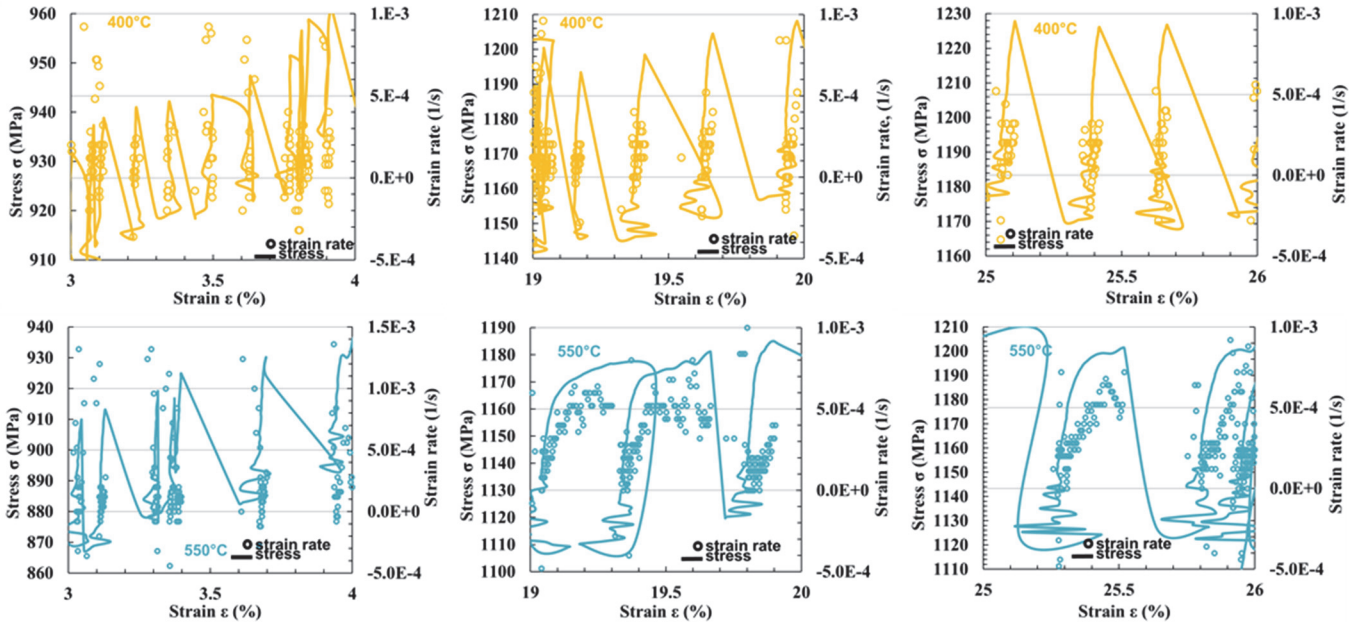

Figure 4: Change in strain rate at the loading sections of the stress-strain curve after the stress drops for 400 and 550 °C. In sections where the load increases between stress drops, the strain rate rapidly increases. The strain rate for 400 and 550°C at the moment of stress drop is approximately constant throughout the entire tensile curve and is equal to approximately $5...9 \cdot 10^{-4}$ sec^{-1}.

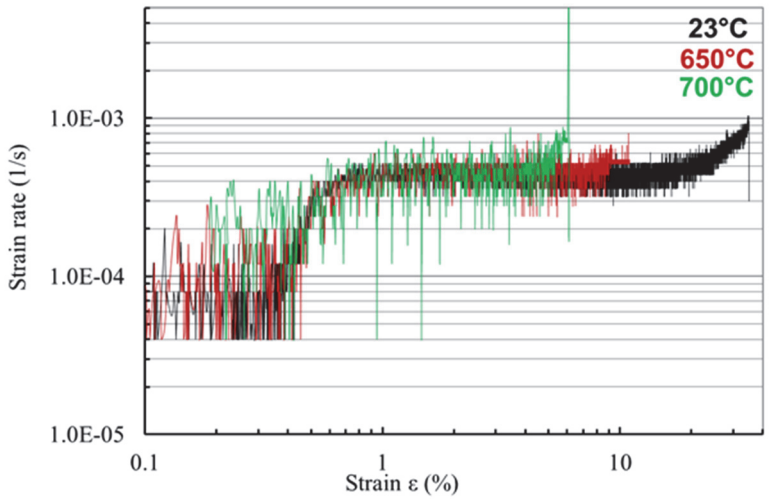

Figure 5: Strain rate at temperatures 23, 650 and 700 °C. For 23, 650, and 700 °C, the strain rate was about $(4...5) \cdot 10^{-4}$ sec^{-1} without serrated flow. It can be seen that for 650 and 700 °C, serrated flow appears in the region of increased strain rate values $6 \cdot 10^{-4}$ sec^{-1} (ε = 8.5 %), and $7 \cdot 10^{-4}$ sec^{-1} (ε = 6 %).

In a hypothetical scenario, the serrated flow phenomenon observed in the tests may be attributed to the pinning of dislocations on ordered regions, followed by the subsequent cluster breaking free. The phenomenon of local reorganization (ordering) of the short-range ordering (SRO) [24,25] Ni-Cr lattice regions, which are present in all Ni-Cr alloys, and the transition to the long-range rhombic (Ni_2Cr) order (LRO) [26,27] are of particular interest. The ordering of SRO is consistent with interatomic distances, while LRO is characterised by the presence of ordering repetition at distances that are not constrained in size. This phenomenon can be attributed to the stronger attraction exhibited by different types of atoms in comparison to identical atoms, within a specific temperature range. This temperature range persists up to the critical temperature, which is situated between 530 and 600°C [28,29]. It is noteworthy that SRO and LRO, as suggested in a number of studies, may be the cause of the previously observed phenomenon of abnormal shrinkage without load application, and "instantaneous elongation" or "strain burst" in nickel-based alloys and EI698-VD in particular [30,31,32]. Moreover, it is known that the temperature-dependent changes in characteristics observed in the tests, namely an increase in the yield stress and a decrease in rupture strain, also occur in LRO. LRO induces a change in the fracture mechanism

from ductile, with coalescence of microvoids in a disordered alloy, to brittle, intergranular fracture in an ordered material. However, additional studies using transmission electron microscopy and X-ray diffraction methods are required to correctly establish the effect of ordering processes in the EI698-VD alloy.

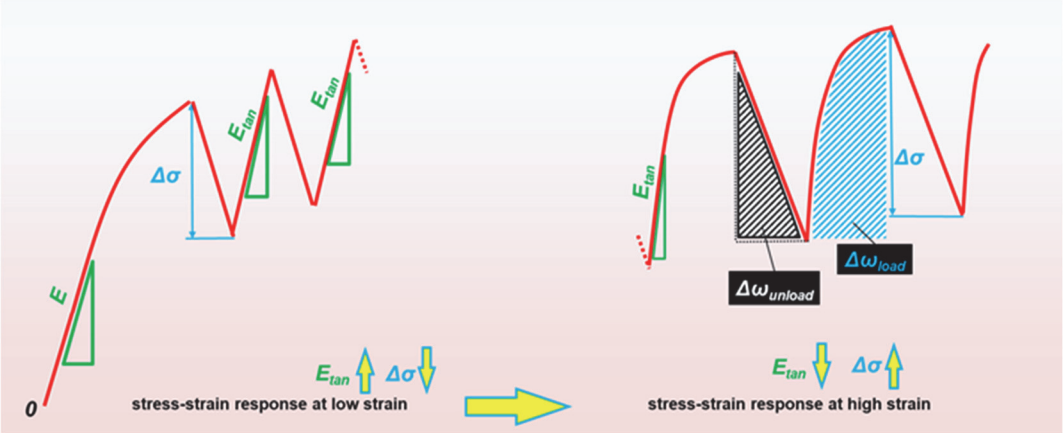

Figure 6: Schematic representation of the experimentally obtained serrated flow. At the initial stage of the elastic-plastic range of the deformation curve, the values of the tangent modulus E_{tan} are close to the Young's modulus E, and stress drops are relatively low. As plastic strains increase, the values of the tangent modulus decrease significantly, and the values of stress drops Δσ increase.

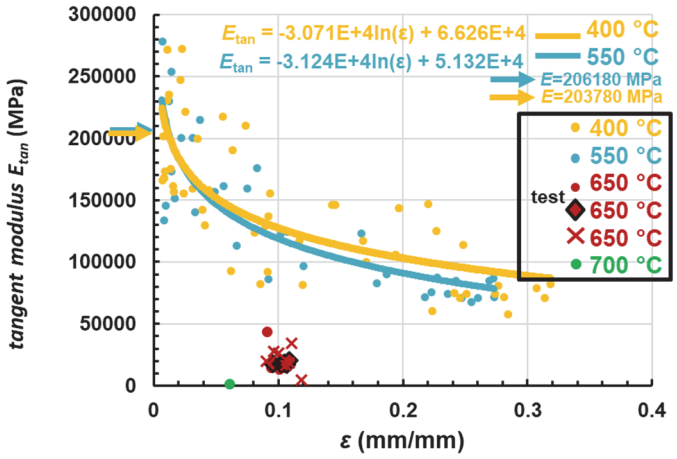

Figure 7: Dependence of tangent modulus E_{tan} values on strain ε under monotonic tension at temperatures 400-700 °C. For temperatures of 650 and 700°C, stress drops appear before rupture. However, the values of the tangent modulus for the load increase sections after stress drops are significantly lower than the values of the Young's modulus.

Tangent modulus

Within the elastic-plastic range of the tensile curve, strain and load drop in alternation with subsequent monotonic loading sections. Subsequent to a drop in load, the tensile curve reveals a slope that is similar to that of the elastic mode. Thus, for low values of accumulated plastic strain, the tangent modulus $E_{tan} = d\sigma/d\varepsilon$ (Figs. 6 and 7) when loading after a load drop is similar in value to the E (Tab. 2) for a given temperature. Then, E_{tan} decreases as the strain ε increases during monotonic tension. The relationship between E_{tan} values and ε can be approximated by a logarithmic function (Fig. 7, Eqn. 4).

$$E_{tan} = B_1 \ln(\varepsilon) + B_2 \tag{4}$$

where $B_1 = -3.071 \cdot 10^4$ MPa, $B_2 = 6.626 \cdot 10^4$ MPa for 400 °C and $B_1 = -3.124 \cdot 10^4$ MPa, $B_2 = 5.132 \cdot 10^4$ MPa for 550 °C are the temperature characteristics. It is a well-known fact that plastic strain is directly implicated in the generation of defects, pores, and cracks in materials. A substantial number of concepts for the evaluation of material degradation (damage) are predicated on alterations in the Young's modulus during fatigue tests or in operational conditions [33]. The tangent modulus is sensitive to the mobility of defects, primarily dislocations, as well as dislocation clusters and structures (cells, walls), grain

boundaries, vacancies, microcracks, and pores (at large strains) [34,35]. The observed change in the values of the tangent modulus E_{tan} (Fig. 7) as the accumulated plastic strain increases can be attributed to the coupled effect of the generation of macro and micro-defects. The tangent modulus decreases in accordance with the principle that, as plastic strain accumulates, the increase in strain is achieved by increasingly easier dislocation movement rather than elastic stretching of the lattice [36,37]. Subsequent to unloading, the material exhibits a high density of mobile dislocations and back stresses. Upon reloading, plastic deformation occurs almost instantaneously. The movement of dislocations is facilitated by internal stresses, thereby reducing the necessary increase in external stress. This results in the same dε requiring less dσ.

Stress drop range

For 400 and 550 °C, the stress drop Δσ (see Fig. 8) on the tensile curve shows three regions with different behavior. At the initial regime of elastic-plastic strain (A regime, Fig. 8), the stress drop Δσ increases rapidly from initial values of 6 and 20 MPa for 400 and 550 °C to 20 and 40 MPa (ε ≈ 0.04, see Fig. 8) at the beginning of the regime of stable Δσ growth (B regime, Fig. 8). When strain values of approximately 0.25 and Δσ = 50 and 80 MPa are reached for 400 and 550 °C, a period of unstable Δσ begins (C regime, Fig. 8) before the specimen ruptures. Actually, during high-temperature testing procedure, the specimen was exposed to cyclic loading with a Δσ stress amplitude at mean stress at the level of the ultimate strength. It should be noted that at a temperature of 400°C, the summary contribution of all $\Delta\omega_{unload}$ (see Fig. 6) (0.0002422…0.1173 MJ·m^{-3}) and $\Delta\omega_{load}$ (0.0004617… 0.04133 MJ·m^{-3}) to the total fracture energy ω_{fe} = 351.91 MJ·m^{-3} (see Tab. 2) is only 9.168 MJ·m^{-3} or 2.54 %.

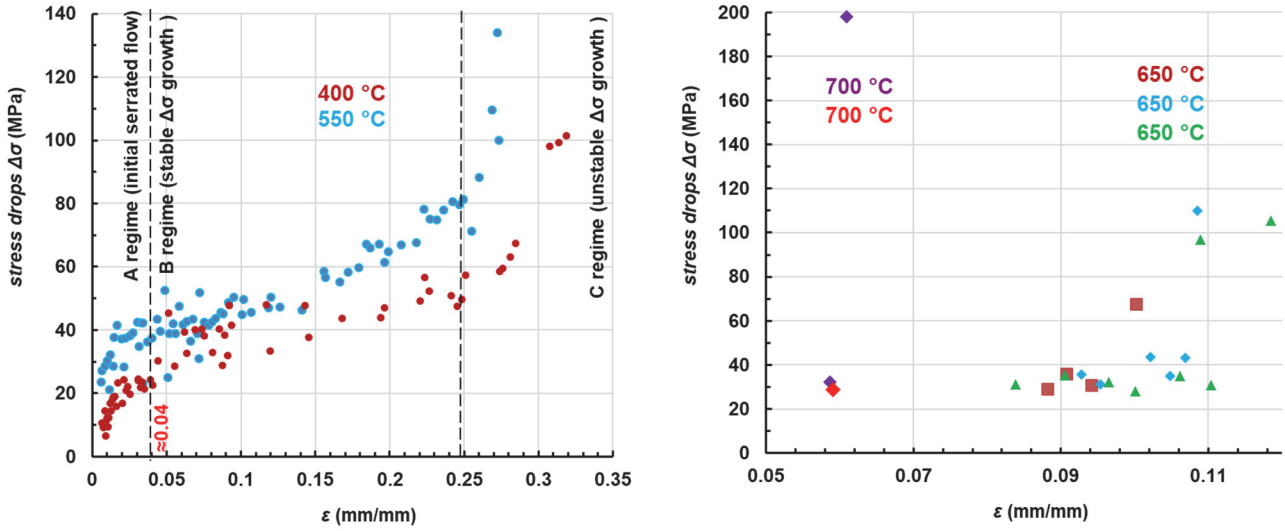

Figure 8: Stress drop range at temperatures 400-700 °C. The stress drop Δσ increases rapidly from the initial elastic-plastic deformation regime A. The B regime corresponds to the stable growth interval of Δσ. A period of unstable Δσ (C regime) begins before the specimen ruptures.

Fracture analysis

The fracture of the specimens was accompanied by the formation of a neck at temperatures between 25 and 550 °C (Figs. 9–11). At temperatures of 25 and 400 °C, two typical zones can be observed in the neck region: the central fibrous zone, where the pores coalesced as they expanded, and the ring-shaped shear lip zone (Figs. 9, 10). In contrast, fracture at higher temperatures of 650 and 700 °C occurred in the absence of localized plastic strain in the neck region, as evidenced in Figs. 12 and 13. Increasing the test temperature of the specimens to 650 and 700 °C resulted in more uniform transverse strain along the gauge length of the specimens.

The 25°C specimen achieved high strain values (see Tab. 2 and Fig. 3) during tensile testing, causing the appearance of intersecting slip lines (Fig. 9). The angle of orientation of the slip lines to the loading axis was found to be 43°7' (Fig. 9, Tab. 3), which corresponded to the plane of maximum shear stress. The fracture surface is typical of the mechanism of ductile generation and coalescence of pores. The circular area in the center of the failure surface is the site of an internal crack formed from a multitude of pores. Multiple surface defects were identified on the cylindrical surfaces of the fractured specimens, located primarily normal to the loading axis or at a small angle above and below the rupture plane.

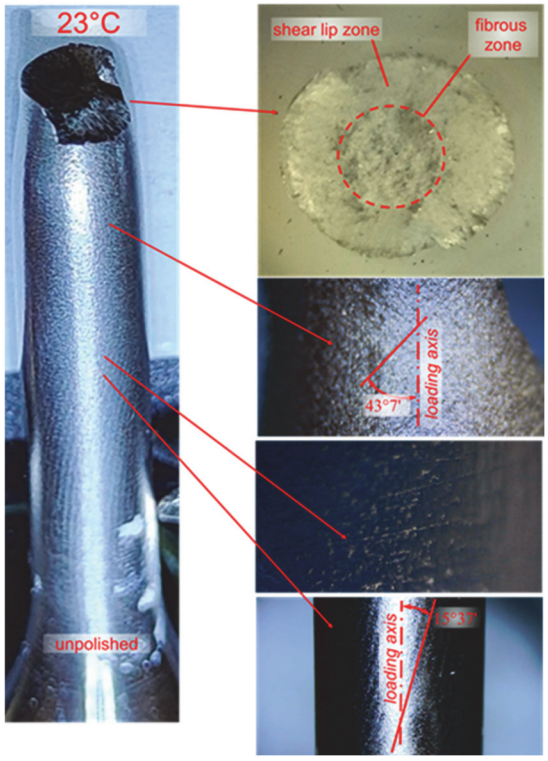

Figure 9: Fractured specimen at a temperature of 25 °C. Surface defects are visible on the specimen. The fracture surface corresponds to ductile rupture. Slip lines intersect in the neck region of the specimen.

A small decrease in plasticity was observed at a temperature of 400 °C (Tab. 2 and Fig. 10). The presence of surface defects became more consistent. However, the fracture mechanism remained ductile. Deformations in the neck occurred in different slip planes at an angle of 43°21' (see Fig. 10, Tab. 3), in the plane of maximum tangential stresses.

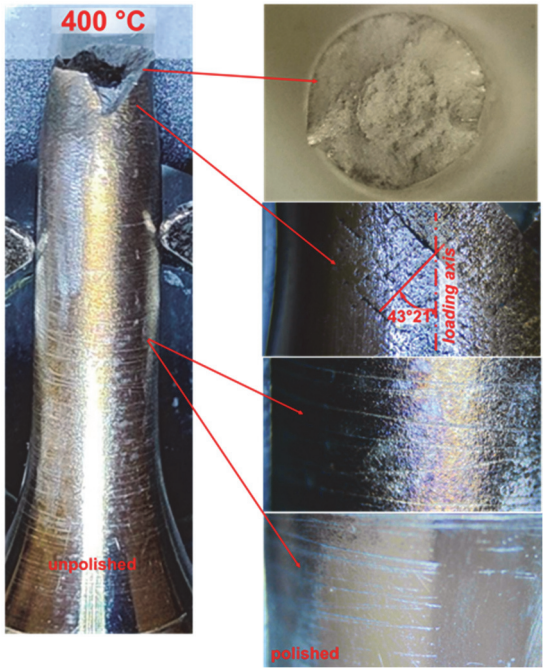

Figure 10: Fractured specimen at a temperature of 400 °C. Surface defects are more significant. The fracture surface corresponds to ductile rupture. Slip lines intersect in the neck region of the specimen.

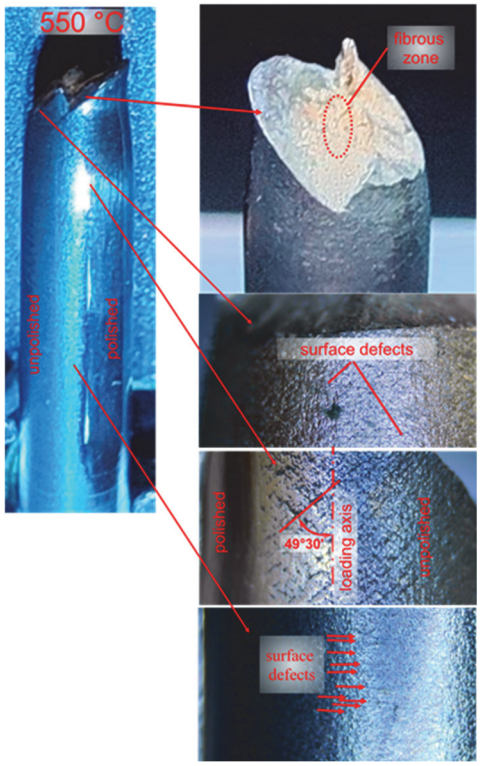

Figure 11: Fractured specimen at a temperature of 550 °C. The slip lines intersect in the neck region of the specimen.

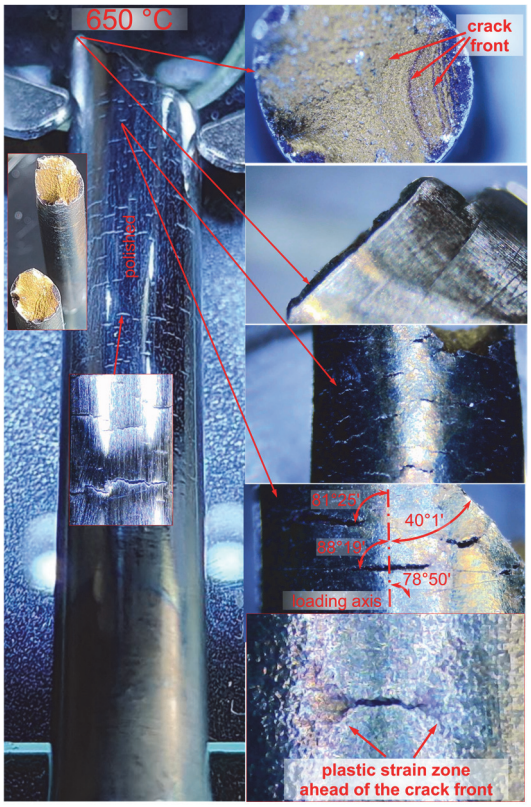

Figure 12: Fractured specimen at a temperature of 650 °C. The surface cracks are oriented along the slip bands. The marks of the plastic strain zones in front of the cracks are approximately the same length as the cracks themselves. Shear fracture is observed between the tips of closely located semi-elliptical surface cracks.

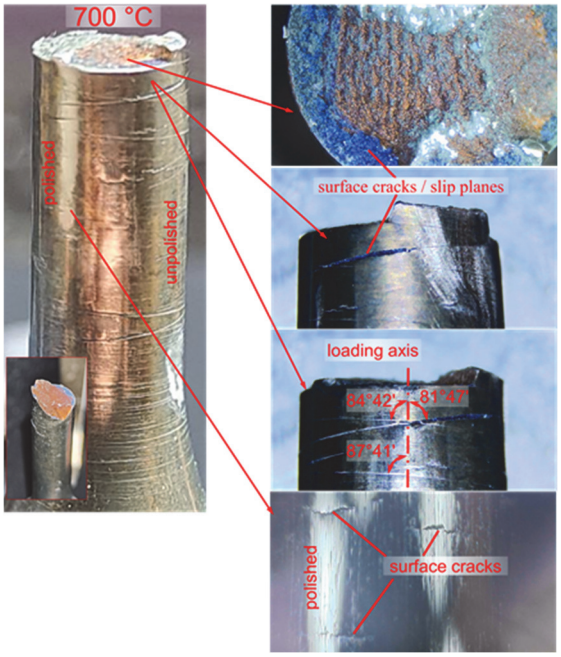

Figure 13: Fractured specimen at a temperature of 700 °C. Large surface cracks are oriented along slip planes.

The behaviour of the alloy at a temperature of 550°C was found to be qualitatively and quantitatively similar to that at 400°C, with a continuing trend toward a moderate decrease in strength and plasticity (Fig. 3, Tab. 2). A ductile mechanism of deformation and fracture was observed. The deformation proceeded at an angle of 49°30' (Fig. 11, Tab. 3) to the loading axis, occurring in two planes. A minor portion of the fracture surface in the central region was found to correspond to the fibrous zone of the ductile formation and coalescence of pores, as observed at lower temperatures. However, the majority of the failure surface was formed by ductile shearing.

At temperatures of 650 and 700 °C, numerous semi-elliptical microcracks and discrete crack fronts marks are observed in the rupture surface. The Figs 12 and 13 show that large cracks at temperatures of 650 and 700 °C are predominantly located at the boundaries of localized slip bands. Additionally, at 650°C, the presence of smaller cracks on the specimen surface oriented perpendicularly to the loading axis is indicative of fracture at the grain boundary [38]. The cause of the transition from transgranular fracture to intergranular fracture [11] in nickel alloys, as is widely attributed to the degradation of cohesive bonds at the grain boundary as a result of the intensification of diffusion and phase changes with increasing temperature. It is also known that non-crystallographic slip bands intensify the formation of macro-cracks and intergranular fracture [39]. Observations made at temperatures of 650 and 700°C reveal the interaction and coalescence of multiple minor cracks on the surface of the specimens (see Figs. 12 and 13). Thus, at 650°C, the fracture of the specimen occurred by a shear in the plane at an angle of 40°1', between surfaces approximately normal to the loading axis of the preceding crack growth, which is an indicator of the action of a mixed mode.

In turn, a rapid decrease in rupture strain at elevated temperatures may be caused by the occurrence of areas of localized elevated strain in the neighborhood of crack fronts, as well as strain bands [40]. Moreover, the true stresses in the neighborhood of such cracks at the moment of rupture are obviously significantly higher than the nominal engineering stresses and true stresses calculated taking into account the area of the specimen diameter in the rupture plane. This can be confirmed by the presence of clearly visible areas of localised intense plastic strain ahead of the fronts of semi-elliptical cracks on the surface of the specimens (Fig. 12). Concurrently, energy parameters, including fracture toughness, may be less influenced by the revealed features due to the comprehensive evaluation of the fracture process. Specimens tested at a temperature of 700°C fractured either in a similar behavior to specimens tested at 650°C, or, in some cases, crack growth was followed by quasi-brittle fracture (Fig. 12 and 13). The bifurcation in this process was controlled by the presence or relative orientation of surface cracks in the neighbourhood of the rupture initiation site.

The slip lines are less visible, which is typical of brittle fracture and comparatively low strain. As illustrated in Figs. 12 and 13, some of the observed cracks are formed from slip bands. The orientation of the shear stresses and slip plane under tension is typically at an angle of 45° to the loading axis. As demonstrated in Tab. 3, a propensity for an increase in the slip angle values was observed as the temperature increased. It is evident that the slip angle exhibited a sensitivity to variations in temperature, concomitant with a decline in plasticity and strength characteristics. For 650 and 700 °C, as illustrated in

Tab. 3, the minimum values for angle measurements are shown, given the variability of these values up to approximately a right angle.

T, °C	Slip plane angle	Mean-square deviation	Fracture mechanism
25	43°7'	2°85'	ductile rupture
400	43°21'	1°34'	ductile rupture
550	49°30'	3°54'	shear fracture
650	> 78°	-	crack growth and shear fracture/brittle failure
700	> 81°	-	crack growth and shear fracture/brittle failure

Table 3: Slip plane angle in tensile-fractured specimens made of alloy EI698-VD.

SEM and EDX analysis

The slip mode in nickel-base alloys is influenced by the composition and the process of heat treatment [38]. In order to identify the factors that may have an effect on the strength, plasticity, and changes in the fracture mechanism of the EI698-VD alloy, the microstructure of the alloy must be analysed. SEM observations of the polished surface of a cut section from the initial state specimen revealed the presence of structural defects not only on the fracture surface, but also in the volume of the primary specimen. The surface in Fig. 14 is oriented perpendicular to the direction of the load.

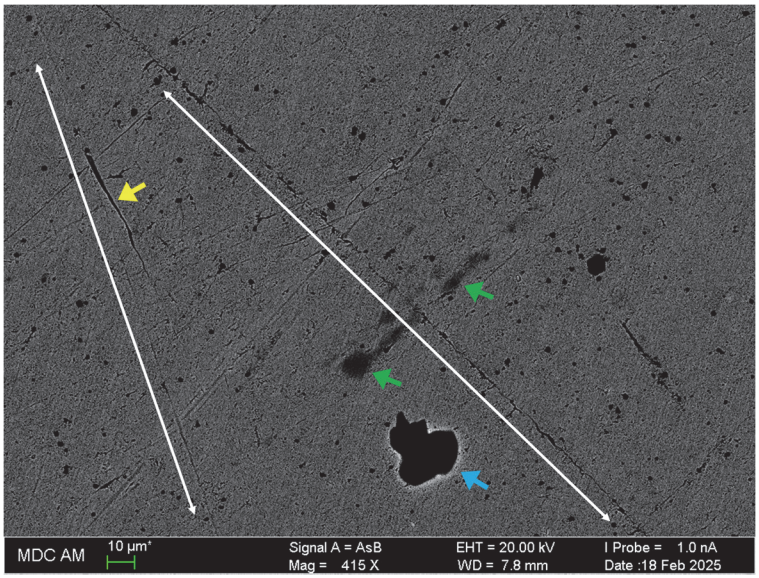

Figure 14: SEM images of the polished virgin microstructure of the EI698-VD alloy. The blue arrow indicates a pore. The yellow arrow indicates a crack. The green arrows indicate C-rich, blurred bands (Fig. 15). The white arrows indicate O, Si, and C-rich crossed chains (red dashed lines in Fig. 15).

The polished surface of the alloy was found to have pores (blue arrow) and microcracks (yellow arrow). The specimen was not subjected to mechanical loading. Therefore, the cracks found can be attributed to solidification cracks and liquation cracks. These cracks typically occur in zones exhibiting the presence of detrimental impurities with a low melting point. EDX analysis revealed a deviation in the chemical composition (Tab. 4) [2] of the surface observed in Fig. 14 from the nominal composition (Tab. 1). The most pronounced disparities are observed in Pb, where the mass fraction was found to be 0.09% (Tab. 4) compared to <0.001% (Tab. 1). Large Pb-rich particles have been observed in Fig. 15. The yellow arrows in Fig. 15 indicate an area characterised by a relative depletion of Ni and an enrichment of Pb, P, Nb, Mo, and Ti. Pb content is incompatible with the heat resistance characteristics. The presence of low-melting-point metals (Pb) in alloys has been shown to result in a significant decrease in strength characteristics at temperatures exceeding 400-600 °C [41,42]. Cracks during the forging, rolling, and welding processes are frequently attributable to the influence of Pb. Pb is not soluble in Ni and is prone to segregation at grain boundaries, which prevents the normal movement of dislocations and initiates intergranular fracture [43]. This may provide a valid explanation for the previously observed steep drop in fracture resistance and the change in fracture mechanism when the temperature increases above 550 °C [3,11].

	W	Cr	Ti	Al	Mo	Fe	Ni	Si	Pb	Nb	Mn
wt.%	0.25	13.27	2.29	1.2	2.57	0.35	68.11	0.61	0.09	1.57	0.07

Table 4: Chemical composition of the EI698-VD alloy polished surface measured using EDX.

EDX mapping in Fig. 15 reveals depleted Ni and enriched O, Si, C bands (red dashed lines) along the chains. In nickel alloys, carbides occur on slip bands [38,44], blocking dislocations, which additionally affects oxidation and increases internal stresses, causing microcracks to appear. In addition, an elevated Si content was identified in the composition of the alloy (0.61% instead of ≤0.5%), accompanied by the presence of Si-rich particles (Fig. 15). SEM analysis of the etched surface of the alloy revealed the presence of spherical, cubic, prismatic, and polygonal particles (Fig. 16). As demonstrated in Fig.15, the spherical and triangular particles (100-200 nm) are enriched in Si and correspond to NiSi, $NiSi_2$ [2,45,46].

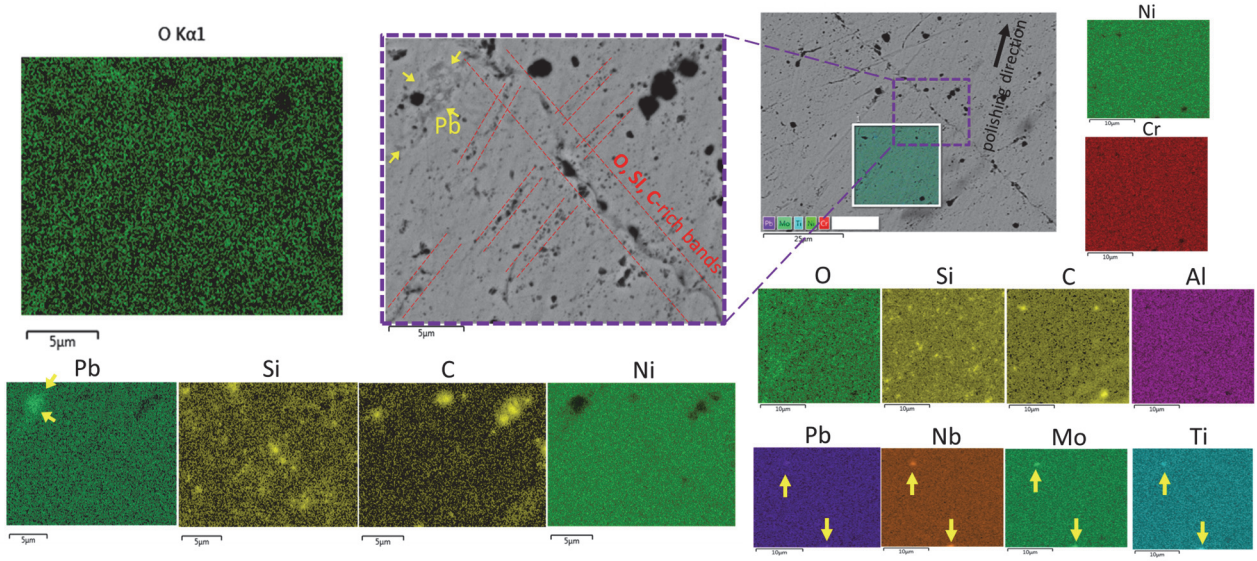

Figure 15: SEM and EDX images of the EI698-VD alloy polished surface. The red dashed lines indicate O, Si, and C-rich crossed chains. The yellow arrow indicates a Pb-rich particles.

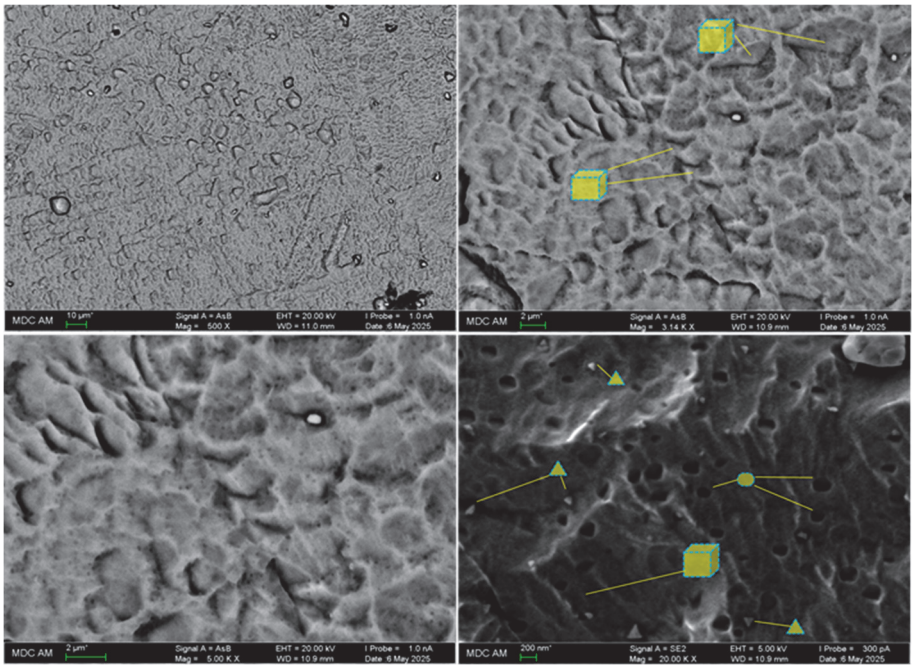

Figure 16: SEM images of the EI698-VD alloy etched surface (Marble reagent). Spherical, cubic, prismatic, and polygonal particles are observed.

It is frequently postulated that methodologies which consider phase change and diffusion processes occurring at the nano- and micro-scale of the material should be utilised to predict the fatigue crack growth rate at elevated temperatures and under thermomechanical loading, as opposed to employing generalised fracture resistance parameters. This study demonstrates that the impact of temperature on fracture mechanisms, as well as the decline in strength and ductility, is qualitatively similar to the previously identified effect of temperature on increasing the fatigue crack growth rate in the EI698-VD alloy [3,11]. Consequently, the damage impact parameter A, determined using a uniaxial monotonic tensile curve, has been demonstrated to predict fatigue crack growth characteristics over a broad range of temperature conditions [3]. The temperature effect on the change in fatigue crack growth resistance under isothermal and thermo-mechanical loading conditions can be characterised using monotonic uniaxial tensile characteristics. This method is less costly compared to data obtained from transmission and scanning electron microscopy, as well as other methods of investigating material structure. Nevertheless, data on the microstructure of alloys is of obvious importance for understanding the mechanisms of the processes involved and improving the characteristics of alloys.

Conclusion

A detailed investigation was performed into the fracture mechanisms of smooth cylindrical specimens made of polycrystalline heat-resistant nickel-based alloy XH73MBTU-VD (EI698-VD) under uniaxial tension in the temperature range of 25–700°C. Both external and internal defects in the alloy structure were identified and described. Observations of the morphology and topology of the alloy microstructure were carried out using SEM and EDX methods. A relationship was established between the features of the deformation process, the fracture mechanism, and the strength and plasticity characteristics. The deviation of the composition of the alloy batch under consideration in this study from the nominal values does not extend the results obtained to specimens and parts of the correct composition.

The high-temperature behaviour characteristics of the alloy with an increased level of detrimental impurities, as identified in the paper, can lead to the unexpected formation of surface defects and cracks, as well as a loss of efficiency and failure of the gas turbine engine.

Below are the summarised results and conclusions of this work.

– It has been demonstrated that elevating the temperature to a level in excess of 550°C results in a substantial decline in the alloy's plasticity. The slope of the slip planes increased with temperature, reaching values of >78° and >81° at 650 and 700°C, respectively;

– At 400 and 550 °C, stress drops $\Delta\sigma$ increased monotonically throughout the elastic-plastic deformation. The tangent modulus E_{tan} values decreased logarithmically with strain. The strain rate increased rapidly in the load increase section after stress drops;

– The fracture initiation site at 25°C and 550°C was an internal crack formed by the mechanism of ductile growth and coalescence of voids. At temperatures of 650 and 700°C, the site of crack nucleation and fracture initiation was surface defects;

– SEM and EDX observations revealed the presence of defects not only on the surface of the fractured specimens, but also in the body of the specimens in their initial state. The Pb content in the alloy was found to exceed the acceptable limit by a factor of 90. It can be hypothesised that the elevated lead Pb content and presence of Pb-rich particles resulted in cracking and a reduction in strength at temperatures in excess of 550°C.

References

[1] Shanyavskiy, A. (2013). Fatigue crack propagation in turbine disks of EI698 superalloy, Fract. Struct. Integrity, 7(24), pp. 13–25. DOI: https://doi.org/10.3221/IGF-ESIS.24.03.

[2] Sulamanidze, A. (2025). Thermal-Induced Inelastic Shrinkage and Swelling Deformation of Heat-Resistant Polycrystalline Nickel-Based Alloy, Adv. Eng. Mater., 27(23), 27:e202502129. DOI: https://doi.org/10.1002/adem.202502129.

[3] Sulamanidze, A., Shlyannikov, V. and Kosov, D. (2024). Prediction of crack growth in polycrystalline XH73M nickel-based alloy at thermo-mechanical and isothermal fatigue loading, Int. J. Fract., 248, pp. 153–177. DOI: https://doi.org/10.1007/s10704-024-00807-1.

[4] Chabina, E.B. (2015). An influence of operational factors on the state of interfaces in high heat-resistant Ni-based alloys intended for GTE discs, Proceedings of VIAM, 8, pp. 13–22.

[5] Sims, C.T., Stoloff, N.S., Hagel W.C. (1987). Superalloys II: High-Temperature Materials for Aerospace and Industrial Power, Wiley-Interscience, New York.
[6] Zrnik, J., Strunz, P., Vrchovinsky,V., Muransky, O., Novy, Z., and Wiedenmann A. (2004). Degradation of creep properties in a long-term thermally exposed nickel base superalloy, Mater. Sci. Eng. A., 387-389, pp. 728–733. DOI: https://doi.org/10.1016/j.msea.2004.02.100 .
[7] Protasova, N.A., Velikanova N.P., Velikanov P.G., Salih, I.S.S., and Akhmadeev, A.A. (2019). Study of Mechanical Properties Stability in the Production of Turbine Disks for Gas Compressor Units, Russ. Aeronaut., 62(4), pp. 675–681. DOI: https://doi.org/10.3103/S1068799819040196 .
[8] Velikanova, N.P. (2009). Statistical analysis of experimental study results on low-cycle fatigue resistance for the EI698-VD high-temperature alloy, Russ. Aeronaut., 52(4), pp. 413–418. DOI: https://doi.org/10.3103/S1068799809040072.
[9] Lomberg, B.S., Bakradze, M.M., Chabina, E.B., Filonova, E.B. (2011). Interrelation between structure and properties of Ni-base superalloys for GTE disks, Aviacionnye materialy and tehnologii, 2(19), pp. 25–30.
[10] Zrník, J., Semeňák, J., Vrchovinský, V., and Wangyao, P. (2001). Influence of hold period on creep–fatigue deformation behaviour of nickel base superalloy, Mater. Sci. Eng. A., 319–321, pp. 637–642. DOI: https://doi.org/10.1016/S0921-5093(01)01030-9.
[11] Shlyannikov, V., Sulamanidze, A., and Kosov, D. (2024). Isothermal and thermo-mechanical fatigue-crack-growth analysis of XH73M nickel alloy, Theor. Appl. Fract. Mech., 129, 104182. DOI: https://doi.org/10.1016/j.tafmec.2023.104182 .
[12] Tumanov, A.V. (2025). Modeling of the transition from transgranular to intergranular fracture at elevated temperatures in EI698 nickel alloy, Fract. Struct. Integrity, 74, pp. 20–30. DOI: https://doi.org/10.3221/IGF-ESIS.74.02.
[13] Shlyannikov, V. and Sulamanidze, A. (2023). Crack tip field analysis for thermo-mechanical fatigue loading, Theor. Appl. Fract. Mech., 125, 103945. DOI: https://doi.org/10.1016/j.tafmec.2023.103945 .
[14] Sulamanidze, A., Shlyannikov, V., Kosov, D. (2023). Verification and validation of multi-physics numerical analysis of thermomechanical fatigue test conditions under induction heating and forced convection, Thermal Sci. Eng. Prog., 45, 102124. DOI: https://doi.org/10.1016/j.tsep.2023.102124 .
[15] 1Metcalfe, E., Nath, B., Wickens, A. (1984). Some effects of the ordering transformation in Nimonic 80A on stress relaxation behaviour, Materials Science and Engineering, 67(2), pp. 157–162. DOI: https://doi.org/10.1016/0025-5416(84)90046-6 .
[16] Vladimirov, S., Kondratenko, M. (2015). The requirements of modern methods of calculating reserves for static strength to mechanical and strength characteristics of liquid-propellant rocket materials, Izvestiya MGTU MAMI., 9, pp. 42-48. DOI: https://doi.org/10.17816/2074-0530-67111.
[17] Maslenkov, S.B. and Maslenkova, E.A. (1991). High-Temperature Steels and Alloys: A Handbook, Moscow, Metallurgiya.
[18] Malygin, G.A. (1992). Anomalous Portvenne–Le Chatelier effect during segregation of interstitial and substitutional impurities at dislocations, Phys. Solid State, 34(8), pp. 2356–2366.
[19] Portevin, A., Le Chatelier F. (1923). Sur un Phenomene Observe lors de l'Essai de Traction d'Alliages en Cours de Transformation, Comptes Rendus de l'Académie des Sciences Paris, 176, pp. 507–510.
[20] Rowlands, B.S., Rae, C., Galindo-Nava, E. (2023). The Portevin-Le Chatelier effect in nickel-base superalloys: Origins, consequences and comparison to strain ageing in other alloy systems, Prog. Mater. Sci., 132, 101038. DOI: https://doi.org/10.1016/j.pmatsci.2022.101038.
[21] Trusov P.V., Chechulina E.A. (2017). Serrated yielding: crystal viscoplastic models, PNRPU mechanics bulletin, 1, pp. 134–163. DOI: https://doi.org/10.15593/perm.mech/2017.1.09.
[22] Yilmaz, A. (2011). The Portevin–Le Chatelier effect: a review of experimental findings, Science and Technology of Advanced Materials, 12(6), 063001. DOI: https://doi.org/10.1088/1468-6996/12/6/063001.
[23] Wojciech, S.O., Grzegorczyk, B., Pawełek, A., Piatkowski, A., Zbigniew, R. (2014). The Portevin –Le Chatelier Effect and Acoustic Emission of Plastic Deformation CuZn30 Monocrystals, Archives of Metallurgy and Materials, 59. DOI: https://doi.org/10.2478/amm-2014-0029.
[24] Hata, S., Matsumura, S., Kuwano, N., Oki, K. (1998). Short range order and its transformation to long range order in Ni4Mo, Acta Mater., 46(3), pp. 881-892. DOI: https://doi.org/10.1016/S1359-6454(97)00314-5.
[25] Wang, Y., Jiang, D., Yu, W., Huang, S., Wu, D., Xu, Y., Yang, X. (2019). Short-range ordering in a commercial Ni-Cr-Al-Fe precision resistance alloy, Mater. Des., 181, 107981. DOI: https://doi.org/10.1016/j.matdes.2019.107981.
[26] Young, G., Tucker, J., Eno, D. (2013). The Kinetics of Long Range Ordering in Ni-Cr Alloys, Conference: 16th International Conference on Environmental Degradation of Materials in Nuclear Power Systems - Water Reactors At: Asheville, NC.

[27] Teng, F., Sprouster, D., Young, G., Ke, J.-H., Tucker, J. (2019). Effect of Stoichiometry on the Evolution of Thermally Annealed Long-Range Ordering in Ni-Cr Alloys, Materialia., 8, pp. 1-11. DOI: https://doi.org/10.1016/j.mtla.2019.100453.
[28] Marucco, A. (1995). Phase transformations during long-term ageing of Ni-Fe-Cr alloys in the temperature range 450–600 °C, Materials Science and Engineering: A., 194(2), pp. 225-233. DOI: https://doi.org/10.1016/0921-5093(94)09668-633.
[29] Marucco, A., Nath, B. (1988). Effects of ordering on the properties of Ni-Cr alloys, J Mater Sci., 23, pp. 2107–2114. DOI: https://doi.org/10.1007/BF01115776.
[30] Klueh, R.L., King J.F. (1979). Unusual creep behavior in a commercial nickel-chromium alloy, Scr. Metall., 13(3), 205-209. DOI: https://doi.org/10.1016/0036-9748(79)90295-3.
[31] Klueh, L., King J.F. (1981). Creep and creep rupture of ERNiCr-3 weld metal, J. Nucl. Mater., 98(1–2), pp. 173-189. DOI: https://doi.org/10.1016/0022-3115(81)90398-6.
[32] Klueh, R.L. (1982). Discontinuous creep in short-range order alloys, Mater. Sci. Eng., 54(1), pp. 65-80. DOI: https://doi.org/10.1016/0025-5416(82)90030-1.
[33] Yu, H. (2009). Variation of elastic modulus during plastic deformation and its influence on springback, Materials & Design, 30, pp. 846-850. DOI: https://doi.org/10.1016/j.matdes.2008.05.064.
[34] Polak, J. (1991). Cyclic plasticity and low cycle fatigue life of metals, Amsterdam, Elsevier.
[35] Li, Q., Hua, G., Lu, H., Yu, B., Li, D. (2018). Understanding the Effect of Plastic Deformation on Elastic Modulus of Metals Based on a Percolation Model with Electron Work Function., JOM., 70, pp. 1130–1135. DOI: https://doi.org/10.1007/s11837-018-2891-3.
[36] Nietsch, J.A., Ott, A.C., Watzl, G. et al. (2025). Comparative study of elastic properties measurement techniques during plastic deformation of aluminum, magnesium, and titanium alloys: application to springback simulation, Meccanica, 60, pp. 55–72. DOI: https://doi.org/10.1007/s11012-024-01918-8.
[37] Luo, L., Ghosh, A.K. (2003). Elastic and inelastic recovery after plastic deformation of DQSK steel sheet, J.Eng.Mater Technol., 125, pp. 237–246. DOI: https://doi.org/10.1115/1.1491574.
[38] Pineau, A., Antolovich S.D. (2009). High temperature fatigue of nickel-base superalloys – A review with special emphasis on deformation modes and oxidation, Eng. Fail. Anal., 16(8), pp. 2668–2697. DOI: https://doi.org/10.1016/j.engfailanal.2009.01.010.
[39] Panin A.V., Kazachenok M.S., Shugurov A.R., Eremina G.M., Smolin A.Yu. (2025). Deformation and fracture of 3D printed Ti-6Al-4V/TiC composites produced by wire-feed electron beam additive manufacturing under uniaxial tensile stress, Fizicheskaya mezomekhanika, 28(S4), pp. 125–142. DOI: https://doi.org/10.55652/1683-805X_2025_28_4_125-142.
[40] Gorbatenko, V.V., Danilov, V.I., Zuev L.B. (2017). Plastic flow instability: Chernov–Luders bands and the Portevin-Le Chatelier effect, Tech. Phys., 62(3), pp. 395–400. DOI: https://doi.org/10.1134/S1063784217030082.
[41] Petersson, C., Szakalos, P., Pettersson R., Lundberg, M. (2025). Effects of liquid metal embrittlement on an alumina forming martensitic steel, Nuclear Materials and Energy, 42, 101907. DOI: https://doi.org/10.1016/j.nme.2025.101907.
[42] Empl, D., Laporte, V., Vincent, E., Dewobroto N., Mortensen A. (2010). Improvement of elevated temperature mechanical properties of Cu–Ni–Sn–Pb alloys, Materials Science and Engineering: A, 527(16–17) pp. 4326-4333. DOI: https://doi.org/10.1016/j.msea.2010.03.056.
[43] Zheng, L., Schmitz, G., Meng, Ye., Chellali, M., Schlesiger, R. (2012). Mechanism of Intermediate Temperature Embrittlement of Ni and Ni-based Superalloys, Critical Reviews in Solid State and Material Sciences, 37, pp. 181-214. DOI: https://doi.org/10.1080/10408436.2011.613492.
[44] Lerch, B.A., Jayaraman, N., Antolovich, S.D. (1984). A study of fatigue damage mechanisms in Waspaloy from 25 to 800°C, Materials Science and Engineering, 66(2), pp. 151–166. DOI: https://doi.org/10.1016/0025-5416(84)90177-0.
[45] Romanyuk K., Cherepanov V., Voigtländer B. (2007). Symmetry Breaking in the Growth of Two-Dimensional Islands on Si(111), Phys. Rev. Lett, 99, 126103. DOI: https://doi.org/10.1103/PhysRevLett.99.126103.
[46] Langkau, S., Wagner, G., Kloess, G., Heuer, M. (2010). TEM analysis of (Ni,Fe)Si_2 precipitates in Si, Phys. Status Solidi A-Appl. Mat., 207, pp. 1832-1844. DOI: https://doi.org/10.1002/pssa.200925309.